INTERNATIONAL JOURNAL FOR NUMERICAL METHODS IN ENGINEERING
Int. J. Numer. Meth. Engng 2007; **69**:2099–2125
Published online 15 August 2006 in Wiley InterScience (www.interscience.wiley.com). DOI: 10.1002/nme.1841

A temperature-related homogenization technique and its implementation in the meshfree particle method for nanoscale simulations

Shaoping Xiao*, †, § and Weixuan Yang‡, ¶

Department of Mechanical and Industrial Engineering and Center for Computer-Aided Design, 3131 Seaman Center, The University of Iowa, Iowa City, IA 52242, U.S.A.

SUMMARY

A new homogenization technique, the temperature-related Cauchy–Born (TCB) rule, is proposed in this paper with the consideration of the free energy instead of the potential energy. Therefore, temperature effects at the nanoscale can be investigated using continuum approximation with the implementation of the TCB rule. The TCB rule is verified via stress analyses of several crystalline solids. Temperature-related material instability is also studied. In addition, a new hierarchical multiscale method is developed through implementing the TCB rule into meshfree particle methods. Quasicontinuum meshfree particle simulations are conducted to investigate bending of nanobeams, crack propagation in nanoplates and a three-dimensional nanoindentation problem. Copyright © 2006 John Wiley & Sons, Ltd.

Received 31 March 2006; Revised 23 May 2006; Accepted 19 June 2006

KEY WORDS: multiscale; temperature; homogenization; material instability; meshfree particle methods

1. INTRODUCTION

Multiscale modelling and simulation of nanostructured materials has been of interest in the area of computational nanotechnology due to the limitations of molecular dynamics. Multiscale methods can be classified into two types: hierarchical multiscale methods and concurrent multiscale methods. Hierarchical multiscale methods employ continuum approximations to approach the nanoscale. A typical hierarchical multiscale method is the quasicontinuum method [1, 2].

*Correspondence to: Shaoping Xiao, Department of Mechanical and Industrial Engineering and Center for Computer-Aided Design, 3131 Seaman Center, The University of Iowa, Iowa City, IA 52242, U.S.A.
†E-mail: shaoping-xiao@uiowa.edu
‡E-mail: weixuan-yang@uiowa.edu
§Assistant Professor.
¶Graduate Student.

Contract/grant sponsor: University of Iowa

As a difference from hierarchical multiscale methods, concurrent multiscale methods couple different length scales, and appropriate numerical methods are employed in various scales to perform simulation simultaneously. Some concurrent multiscale methods [3–5] couple the continuum model and the molecular model. Although multiscale methods have potential to simulate large nano systems, most currently proposed multiscale methods still have limitations in length/time scales and some difficulties in developing physical-based models.

Whether hierarchical or concurrent multiscale methods are used for modelling crystalline solids, continuum approximation is conducted through a homogenization technique such as the Cauchy–Born (CB) rule [6, 7]. The CB rule assumes that there are locally homogeneous deformations in the continuum domain so that the constitutive relation is derived from atomic-level potential. Consequently, the homogenization technique provides a link between molecular and continuum models. However, the continuum model is usually assumed to be at a zero temperature. As a result, temperature effects at the nanoscale cannot be investigated via most currently existed continuum approximation. It has been shown that most physical phenomena of nanoscale materials and devices [8, 9], particularly material failure and damping in devices, are temperature dependent. Therefore, a temperature-related homogenization technique is needed to enhance multiscale/multiphysics models.

One of the ways to introduce temperature effects is to employ potential that incorporate entropy due to lattice vibration, for example, a local Einstein description [10] that is conceptually similar to the coarse graining of vibrations in first-principles thermodynamics [11]. Shenoy *et al*. [12] and Dupuy *et al*. [13] implemented a free energy minimization technique in the quasicontinuum method, while Diestler and co-workers [14, 15] calculated isotropic stresses using the pseudoatomic Hamiltonian. In this paper, we propose a new homogenization technique, called the temperature-related Cauchy–Born (TCB) rule, for the continuum model in multiscale methods. Using the work of Shenoy *et al*. [12] and Diestler *et al*. [14, 15] as a referent, we consider the Helmholtz free energy, i.e. the effective energy in References [12, 14, 15]. Consequently, in the continuum domain the energy contains not only the potential energy due to deformation of molecular structures but also the thermal energy due to vibration of atoms. A stress–strain relation is given in the paper as a generalized constitutive law that can be employed in the continuum model of multiscale methods.

Finite element (FE) methods [16] based on the quasicontinuum approach are often used to model continua in both hierarchical and concurrent multiscale methods. Compared with conventional FE methods, meshfree particle (MP) methods [17, 18] are more attractive for use in a variety of applications [19–21], including problems involving moving boundaries, discontinuities, and extremely large deformations. Belytschko and co-workers [22–24] performed stability analysis of meshfree particle methods and concluded the meshfree particle methods with Lagrangian kernels and stress points are stable methods. Given the advantages of meshfree particle methods, their incorporation with a homogenization procedure will significantly benefit multiscale methods.

The outline of this paper is as follows: A new homogenization technique, the TCB rule, is described in Section 2. Verification of the TCB rule is conducted in Section 3 via stress analyses of two- and three-dimensional molecular structures. Temperature-related material stability analysis is performed in Section 4 to demonstrate temperature effects on material instability. Section 5 introduces meshfree particle methods, including their stability characteristics and integration schemes. In Section 6 quasicontinuum meshfree particle methods are developed via the implementation of the TCB rule. A cohesive crack model is also described so that crack propagation at the nanoscale can be simulated using quasicontinuum meshfree particle methods. Several examples are studied in Section 7 followed by the conclusions.

DOI: 10.1002/nme

2. TEMPERATURE-RELATED CAUCHY–BORN (TCB) RULE

2.1. Cauchy–Born (CB) rule

Generally, in a nanoscale continuum model, the potential energy depends on the elongations and angle changes of the atomic bonds underlying the discretized continuum domain via the conventional CB rule [6, 7]. The CB rule states that the deformation is locally homogeneous. Therefore, the atomic-level lattice follows the deformation given by the macroscopically imposed deformation gradient. For example, an undeformed lattice vector $\mathbf{A}$ in the reference configuration can be mapped into a deformed lattice vector $\mathbf{a}$ in the current configuration via

$$\mathbf{a} = \mathbf{F}\mathbf{A}, \quad \mathbf{F} = \frac{\partial \mathbf{x}}{\partial \mathbf{X}} \tag{1}$$

where $\mathbf{F}$ is the gradient of deformation, $\mathbf{x}$ are Eulerian co-ordinates and $\mathbf{X}$ are Lagrangian co-ordinates. Consequently, the total potential energy, also called the strain energy of the continuum model, in the reference configuration Ω_0 is defined by

$$W^C = \int_{\Omega_0} w_C(\mathbf{F})\, \mathrm{d}\Omega_0 \tag{2}$$

where w_C is the strain energy per unit volume. Based on non-linear continuum mechanics [16], the first Piola–Kirchhoff stress, $\mathbf{P}$, is obtained from the first derivative of the strain energy density to the gradient of deformation

$$\mathbf{P} = \frac{\partial w_C(\mathbf{F})}{\partial \mathbf{F}} \tag{3}$$

The above equation usually serves as a constitutive relation implemented into continuum models in either hierarchical or concurrent multiscale modelling of crystalline solids. For many important situations such as in single-layer curved crystalline sheets, the exponential CB rule [25, 26] was developed so that the deformation gradient can map the tangent space of the undeformed surface to the one of the deformed surface.

2.2. Temperature-related Cauchy–Born (TCB) rule

In the TCB rule, we consider the Helmholtz free energy, i.e. the effective energy in References [12–15], rather than the potential energy at the nanoscale. To obtain reasonable accuracy for the Helmholtz free energy calculation in the nanoscale continuum model, the motion of an atom in a solid is assumed to be harmonic [27]. We also neglect coupled vibration of different atoms. Consequently, the atomic-level free energy, F_H, of a crystalline solid, which contains N atoms at a temperature of T, is expressed as [27]

$$F_H = \varphi(\mathbf{x}) + \kappa_\mathrm{B} T \sum_j \ln\left[2\sinh\left(\frac{\hbar\omega_j}{2\kappa_\mathrm{B} T}\right)\right] \tag{4}$$

where $\varphi(\mathbf{x})$ is the potential energy of the atoms in their equilibrium positions, $\mathbf{x}$, at a temperature of 0 K; $\hbar = h/2\pi$, h is Planck's constant; κ_B is the Boltzmann constant. The sum over j includes

DOI: 10.1002/nme

all the non-zero vibrational modes of the system. The frequencies, ω_j, are eigenvalues of the dynamic matrix, **D**, which is calculated as

$$D_{I\alpha J\beta} = \frac{1}{\sqrt{m_I m_J}} \left(\frac{\partial^2 \varphi}{\partial x_{I\alpha} \partial x_{J\beta}} \right) \tag{5}$$

where $x_{I\alpha}$ is the vibrational co-ordinate in direction α for atom I, and m_I is the mass of atom I.

We take a local harmonic model [28] in this paper so that the principal frequencies of atom I can be calculated by diagonalizing the local dynamic matrix whose determinant is expressed as $\overline{D}_I = (\prod_j^n \omega_{Ij})^2$. Therefore, (4) can be simplified as

$$F_H = \varphi(x) + n\kappa_B T \sum_j \ln \left(\frac{\hbar \overline{D}_I^{1/2n}}{\kappa_B T} \right) \tag{6}$$

where n is the number of degrees of freedom per atom. In the continuum approach to a crystalline solid with the TCB rule, we assume that atoms not only have locally homogeneous deformation as in the conventional CB rule but also have the same vibration mode locally [29] at a given temperature. Therefore, all the local atoms have the same dynamic matrix that is a function of the deformation gradient.

In summary, the proposed TCB rule assumes: (1) atoms have locally homogeneous deformation; (2) atoms have the same local vibration modes; (3) the vibration of an atom is harmonic; and (4) coupled vibration of different atoms is negligible. In the continuum model of a crystalline solid that contains N atoms at a temperature field of $T(\mathbf{X})$, the total free energy, W_H, is written as

$$\begin{aligned} W_H(\mathbf{F}, T) &= \int_{\Omega_0} w_C(\mathbf{F})\, \mathrm{d}\Omega_0 + n\kappa_B \int_{\Omega_0} \rho_n T \ln \left[\frac{\hbar (\overline{D}(\mathbf{F}))^{1/2n}}{\kappa_B T} \right] \mathrm{d}\Omega_0 \\ &= \sum_i^{N_q} w_C(\mathbf{F}_i^q) A_i + n\kappa_B \sum_i^{N_q} n_i^q T_i^q \ln \left[\frac{\hbar (\overline{D}(\mathbf{F}_i^q))^{1/2n}}{\kappa_B T_i^q} \right] \end{aligned} \tag{7}$$

where ρ_n is the number of atoms per unit volume; N_q is the number of quadrature points in the continuum model; and A_i is the volume associated with one quadrature point, X_i^q, which represents n_i^q atoms. The first term on the RHS of the above equation is the continuum level strain energy when temperature is equal to zero. In the continuum model, the deformation gradient and the temperature are evaluated at each quadrature point. With the TCB technique, all the bonds and atoms in A_i are assumed to be at the same deformation and the same temperature. Consequently, the strain energy density, w_C, and the dynamic matrix can be calculated using the unit cell model for each quadrature point.

As a difference from other research [12–15], we modify (3) to calculate the continuum-level first Piola–Kirchhoff stress for continuum approach to finite-temperature nano systems as follows:

$$\mathbf{P}(\mathbf{F}, T) = \frac{\partial w_H(\mathbf{F}, T)}{\partial \mathbf{F}} \tag{8}$$

where w_H is the free energy density, and it is a function of the deformation gradient and the temperature. Equation (8) can serve as a temperature-dependent constitutive relation that can be

DOI: 10.1002/nme

implemented in most hierarchical and concurrent multiscale methods to investigate temperature-related physical behaviour of nanostructured materials

3. VERIFICATIONS OF THE TCB RULE

To verify the proposed TCB rule, we perform stress analyses of various crystalline solids at any given deformation gradient and temperature using the continuum approximation with the TCB rule. Then, we compare the continuum-level Cauchy stresses with the atomic-level ones from molecular simulations. It should be noted here that the simulated objects are assumed to be canonical ensembles subject to any given deformation and temperature. Either the Monte Carlo method or molecular dynamics can be used to obtain the same stress state in the canonical ensemble at thermodynamic equilibrium within any given boundary condition. In this paper, we employ molecular dynamics with the periodic boundary conditions and the Berendsen thermostat [30]. The atomic-level Cauchy stresses [31], $\boldsymbol{\sigma}^A$, of the simulated object is calculated via

$$\boldsymbol{\sigma}^A = \frac{1}{V}\sum_I \left(\frac{1}{2} \sum_{J(\neq I)} \mathbf{r}_{IJ} \otimes \mathbf{f}_{IJ} \right), \quad \mathbf{f}_{IJ} = \frac{\partial \varphi(r_{IJ})}{\partial r_{IJ}} \frac{\mathbf{r}_{IJ}}{r_{IJ}} \tag{9}$$

where V is the total volume; $\mathbf{r}_{IJ}$ $(= \mathbf{r}_J - \mathbf{r}_I)$ and $\mathbf{f}_{IJ}$ represent the interatomic distance and force between atoms J and I, respectively; $\otimes$ denotes the tensor product of two vectors. The sign convention adopted here for $\mathbf{f}_{IJ}$ that is positive for attraction and negative for repulsion. Accordingly, a positive stress indicates tension and a negative stress indicates compression.

When employing the continuum approximation with the TCB rule, the first Piola–Kirchhoff stress, $\mathbf{P}$, is calculated via (8). Then, the continuum-level Cauchy stress, $\boldsymbol{\sigma}^C$, is computed [16] as

$$\boldsymbol{\sigma}^C = J^{-1}\mathbf{F} \cdot \mathbf{P}^{\mathrm{T}}, \quad J = \det(\mathbf{F}) \tag{10}$$

where J is the determinant of deformation gradient $\mathbf{F}$.

3.1. Two-dimensional triangular lattice

A two-dimensional crystalline plate with the triangular lattice, as shown in Figure 1, is considered first. This nanoplate contains 1116 atoms, and its length and width are 30 nm, respectively. Each atom has a mass of 12 amu. We employ the following Lennard–Jones 6–12 potential function to describe the interatomic interaction between nearest neighboured atoms

$$\varphi(l) = 4\varepsilon \left[\frac{1}{4} \left(\frac{l_0}{l} \right)^{12} - \frac{1}{2} \left(\frac{l_0}{l} \right)^{6} \right] \tag{11}$$

where l is the deformed bond length, $l_0 = 1$ nm is the undeformed bond length, and $\varepsilon = 8.25$ aJ is the depth of the energy well.

Based on the assumption of the TCB rule, when the nanoplate is subjected to a deformation gradient, $\mathbf{F} = \begin{bmatrix} F_{11} & F_{12} \\ F_{21} & F_{22} \end{bmatrix}$, and a finite temperature, all the unit cells (shown in Figure 1) are deformed identically, and all the atoms have the same harmonic vibration mode. Therefore, the strain energy density at the temperature of 0 K is calculated from the potential of the unit cell. The dynamic

DOI: 10.1002/nme

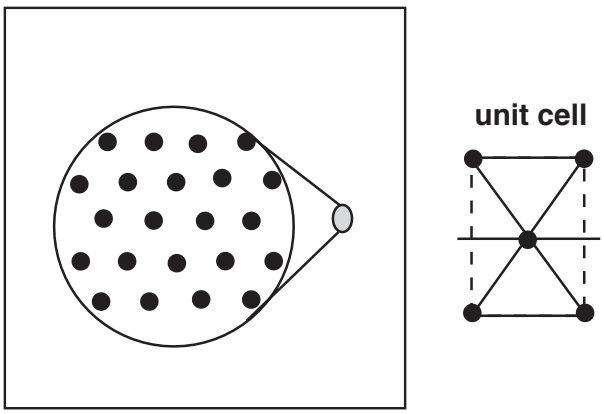

Figure 1. A two-dimensional Lennard–Jones crystal with a triangular lattice.

matrix of the atom located in the centre of the unit cell can also be computed. They are:

$$w_C = \frac{2}{\sqrt{3}l_0}[\varphi(l_1) + \varphi(l_2) + \varphi(l_3)] \tag{12}$$

$$D_{ij} = \sum_{k=1}^{3} \left[\varphi''(l_k) r_{ki} r_{kj} \left(\frac{l_0}{l_k}\right)^2 - \varphi'(l_k) r_{ki} r_{kj} \frac{l_0^2}{l_k^3} + \frac{\varphi'(l_k)}{l_k} \delta_{ij} \right] \tag{13}$$

where $l_k = l_0\sqrt{r_{k1}^2 + k_{k2}^2}$ $(k = 1, 2, 3)$ and

$$r_{11} = F_{11}, \quad r_{12} = F_{12}, \quad r_{21} = \tfrac{1}{2}F_{11} - \tfrac{\sqrt{3}}{2}F_{12}$$

$$r_{22} = \tfrac{1}{2}F_{21} - \tfrac{\sqrt{3}}{2}F_{22}, \quad r_{31} = \tfrac{1}{2}F_{11} + \tfrac{\sqrt{3}}{2}F_{12}, \quad r_{32} = \tfrac{1}{2}F_{21} + \tfrac{\sqrt{3}}{2}F_{22}$$

The atomic-level and continuum-level Cauchy stresses are computed via (9) and (10) for any given deformation gradient and temperature. Figure 2 shows the comparison of each component of Cauchy stresses at various temperatures when two different deformation gradients are given. We also calculate Cauchy stresses using the continuum model with the conventional CB rule to demonstrate the advantages of the TCB rule. The continuum approximation with the conventional CB rule gives constant stresses at different temperatures since temperature effects are not considered in the CB rule. If temperature effects are considered, the continuum-level normal stresses, calculated based on the TCB rule, decrease with the increasing temperature due to thermal expansion. The results agree with the molecular dynamics solutions. Shear stresses calculated from continuum approximations with either the conventional CB or the TCB rule are supported by molecular dynamics simulation because temperature has no effects on shear stresses.

3.2. Graphene sheet

As a more practical example, we consider temperature effects on stress analysis of a graphene sheet. Figure 3 shows the honeycomb multi-lattice of a graphene sheet with its unit cell in the

DOI: 10.1002/nme

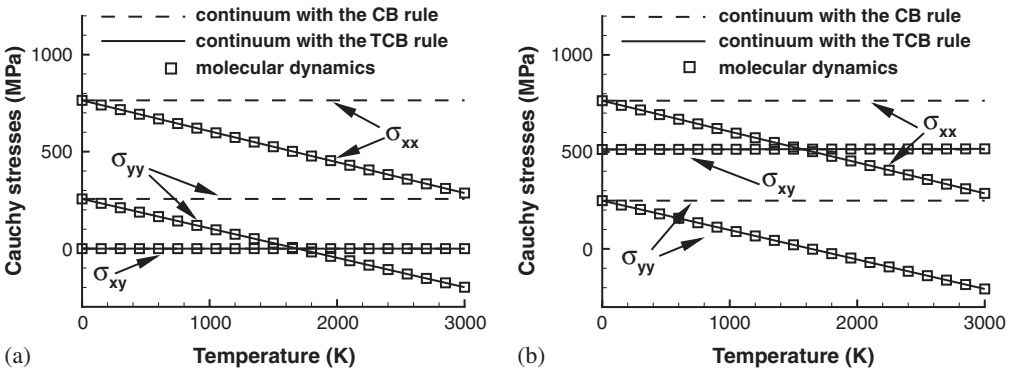

Figure 2. Comparison of Cauchy stress components at various temperatures in a two-dimensional Lennard–Jones crystal subjected to the following deformation gradients: (a) $F_{11} = 1.001$, $F_{12} = F_{21} = 0.0$, $F_{22} = 1.0$; and (b) $F_{11} = 1.001$, $F_{12} = 0.002$, $F_{21} = 0.0$, $F_{22} = 1.0$.

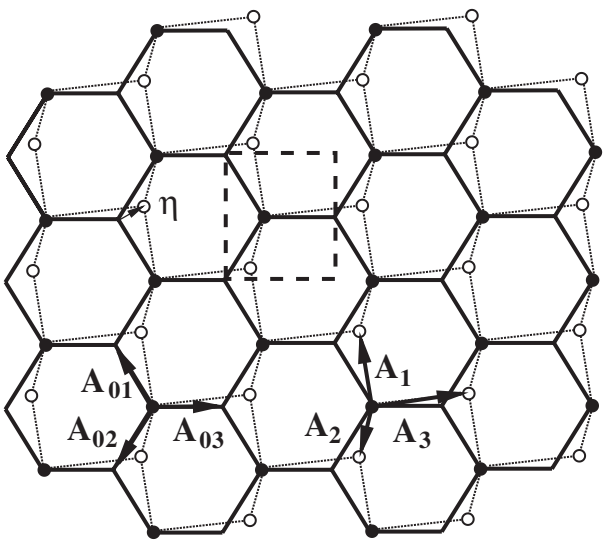

Figure 3. A graphene sheet and its unit cell.

dashed box. There are three inequivalent bonds, $\mathbf{A}_{0i}$ $(i = 1, 2, 3)$ in the reference configuration, i.e. the undeformed configuration. It should be noted that the graphene sheet is a Bravais multi-lattice with two basic nuclei: a black dot and a white dot shown in Figure 3. Consequently, when the graphene sheet is subjected to a homogeneous deformation, one cannot use only one basic nuclei and two simple Bravais lattice vectors to define the entire lattice. Therefore, a shift vector, $\boldsymbol{\eta}$, known as the inner displacement [32], must be introduced as shown in Figure 3 to define the relative displacement of the basic nuclei. The inner displacement represents an internal model of deformation in the unit cell instead of the homogeneous deformation sustained by the entire

DOI: 10.1002/nme

graphene sheet. Then, the deformed lattice vectors $\mathbf{A}_i$ is written as

$$\mathbf{A}_i = \mathbf{A}_{0i} + \boldsymbol{\eta} \tag{14}$$

Since inner displacements are in the internal equilibrium, we neglect the temperature effects on inner displacements. Similar to Reference [32], the inner displacement is calculated by minimizing the strain energy density with respect to $\boldsymbol{\eta}$ for a given deformation of the lattice, i.e.

$$\boldsymbol{\eta}(\mathbf{F}) = \arg\left(\min_{\boldsymbol{\eta}} w_C(\mathbf{F}, \boldsymbol{\eta})\right) \Rightarrow \left.\frac{\partial w_C(\mathbf{F}, \boldsymbol{\eta})}{\partial \boldsymbol{\eta}}\right|_{\mathbf{F}} = 0 \tag{15}$$

When a graphene sheet is subjected to a homogeneous deformation and a particular temperature, the positions of the atoms in the current configuration, i.e. the deformed configuration, are expressed in terms of the deformation gradient $\mathbf{F}$ and the inner displacement $\boldsymbol{\eta}$. Therefore, the total free energy of the graphene sheet is computed as

$$W_H(\mathbf{F}, \boldsymbol{\eta}, T) = A w_C(\mathbf{F}, \boldsymbol{\eta}) + N\kappa_{\mathrm{B}} T \ln\left[\frac{\hbar(\overline{D}(\mathbf{F}, \boldsymbol{\eta}))^{1/2n}}{\kappa_{\mathrm{B}} T}\right] \tag{16}$$

where A is the area of the simulated graphene sheet, and N is the total carbon atoms. Equations (8) and (10) are thereafter employed to calculate the continuum-level Cauchy stress.

In this example, we consider a graphene sheet containing 800 atoms to be subjected to a deformation gradient of $\mathbf{F} = \begin{bmatrix} 1.02 & -0.01 \\ 0.0 & 1.00 \end{bmatrix}$. In our calculation, we use a modified Morse potential function [33] as follows to describe the interatomic interaction:

$$\begin{aligned} E &= E_{\text{stretch}} + E_{\text{angle}} \\ E_{\text{stretch}} &= D_e\{[1 - \mathrm{e}^{-\beta(r-r_0)}]^2 - 1\} \\ E_{\text{angle}} &= \tfrac{1}{2}k_\theta(\theta - \theta_0)^2[1 + k_s(\theta - \theta_0)^4] \end{aligned} \tag{17}$$

where E_{stretch} is the bond energy due to bond stretching or compressing, E_{angle} is the bond energy due to bond angle-bending, r is the current bond length, and θ is the angle of two adjacent bonds representing a standard deformation measure in molecular mechanics. The parameters are:

$$\begin{aligned} &\beta = 2.625 \times 10^{19}\,\mathrm{nm}^{-1}, \quad D_e = 0.603105\,\mathrm{aJ} \\ &r_0 = 0.142\,\mathrm{nm}, \quad \theta_0 = 2.094\,\mathrm{rad} \\ &k_\theta = 1.13\,\mathrm{aJ/rad}^2, \quad k_s = 0.754\,\mathrm{rad}^{-4} \end{aligned} \tag{18}$$

The calculated normal Cauchy stresses from molecular dynamics and the continuum approximation with either the conventional CB rule or the TCB rule are compared in Figure 4. We can also conclude that the continuum-level Cauchy stresses based on the continuum approximation with the TCB rule are in good agreement with those from molecular dynamics at various temperatures.

DOI: 10.1002/nme

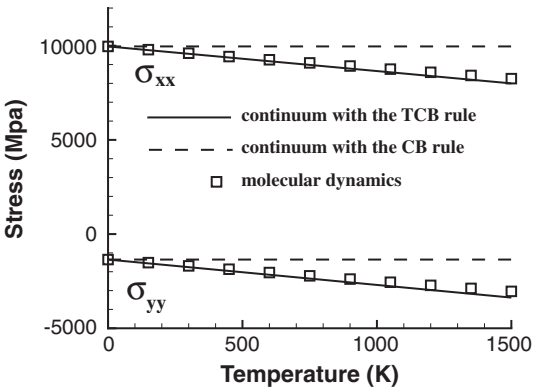

Figure 4. Normal Cauchy stresses of a graphene sheet subject to a deformation gradient of $F_{11} = 1.02$, $F_{12} = -0.01$, $F_{21} = 0.0$ and $F_{22} = 1.00$.

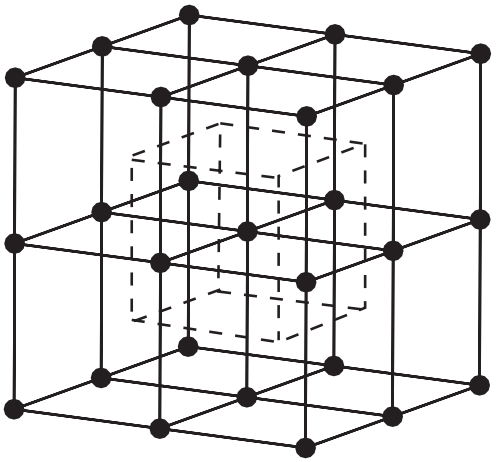

Figure 5. Geometry of a simple cubic lattice and the unit cell (dash lines).

3.3. Three-dimensional simple cubic lattice

A three-dimensional simple cubic lattice with each dimension of 5 nm is studied in this example. Figure 5 shows the basic geometry of this cubic lattice and its unit cell. We also employ the Lennard–Jones 6–12 potential and the parameters are the same as in (11).

To include a large range of temperatures, we investigate the Cauchy stress evolution in the simulated lattice at various temperatures from 0 to 1500 K, subject to the following deformation gradient:

$$\mathbf{F} = \begin{bmatrix} 1.01 & 0.05 & 0.03 \\ 0.0 & 1.02 & 0.04 \\ 0.0 & 0.0 & 1.03 \end{bmatrix} \tag{19}$$

DOI: 10.1002/nme

Table I. Comparison of normal Cauchy stresses (MPa) at various temperatures for a three-dimensional simple cubic lattice subjected to the deformation gradient in (19).

Temperature		0 K	300 K	900 K	1500 K
σ_{xx}	CB	5128.15	5128.1	5128.15	5128.15
	TCB	5128.15	5092.4	5021.12	4949.77
	MD	5128.15	5083.5	5043.26	4998.69
σ_{yy}	CB	9734.92	9734.9	9734.92	9734.92
	TCB	9734.92	9695.0	9615.35	9535.63
	MD	9734.92	9703.5	9632.53	9569.72
σ_{zz}	CB	13 035.5	13 035.0	13 035.5	13 035.5
	TCB	13 035.5	12 991.0	12 903.8	12 815.9
	MD	13 035.5	13 007.0	12 936.4	12 860.7

Since there are no temperature effects on shear stresses, we only compare the normal Cauchy stresses from molecular dynamics simulation and those from the continuum approximation with either the CB rule or the TCB rule as shown in Table I. With the consideration of temperature effects, the results from the continuum approximation with the TCB technique match the molecular dynamics solutions better than those from the continuum approximation with the CB rule.

4. TEMPERATURE-DEPENDENT MATERIAL STABILITY

4.1. Material stability analysis with the TCB rule

At the nanoscale, material failure is temperature dependent. With the proposed TCB rule, we study temperature effects on material stability using a linearized stability analysis technique [24]. In order to conduct a stability analysis, we first derive the linearized equations. Assume perturbations in the displacement

$$\overline{\mathbf{u}} = \mathbf{u} + \widetilde{\mathbf{u}} \tag{20}$$

where the superposed $\sim$ denotes the perturbation. In general, assume that the perturbation of displacements is in the form of a plane wave

$$\widetilde{\mathbf{u}} = \mathbf{g}\, \mathrm{e}^{\mathrm{i}\omega t + \mathrm{i}\kappa \mathbf{n}^0 \cdot \mathbf{X}} \tag{21}$$

where $\mathbf{g}$ is polarization of the wave, κ is wave number, ω is frequency and $\mathbf{n}^0$ is the normal direction of the wave front with respect to the initial configuration.

The perturbation solutions are governed by the following perturbed governing equations:

$$\rho_0 \ddot{\widetilde{\mathbf{u}}} = \nabla_{\mathbf{X}} \cdot \widetilde{\mathbf{P}}^{\mathrm{T}} \tag{22}$$

where ρ_0 is the initial density, $\nabla_{\mathbf{X}}$ is the gradient with respect to the material co-ordinate $\mathbf{X}$ and the superposed dots denote material time derivatives.

DOI: 10.1002/nme

The perturbed first Piola–Kirchhoff stress tensor is

$$\widetilde{P}_{ij} = \overline{C}_{ijkl}\widetilde{F}_{kl} \tag{23}$$

where $\overline{C}_{ijkl}$ is the first tangential stiffness tensor, and it is

$$\overline{C}_{ijkl} = \frac{\partial^2 w_H(\mathbf{F}, T)}{\partial F_{ij}\,\partial F_{kl}} \tag{24}$$

Then, the perturbed equation, (22), yields

$$\omega^2 g_i - \frac{\kappa^2}{\rho_0}\overline{C}_{jikl}n_j^0 n_l^0 g_k = 0 \tag{25}$$

or

$$\det\left[\omega^2\delta_{ik} - \frac{\kappa^2}{\rho}\overline{C}_{jikl}n_j^0 n_l^0\right] = \det\left[\omega^2\delta_{ik} - \frac{\kappa^2}{\rho_0}A_{ik}\right] = 0 \tag{26}$$

where $A_{ik} = \overline{C}_{jikl}n_j^0 n_l^0$ is the acoustic tensor.

The strong ellipticity condition can be expressed as

$$\overline{C}_{jikl}n_j^0 n_l^0 h_i h_k > 0 \quad \forall \mathbf{h} \text{ and } \mathbf{n}^0 \tag{27}$$

In other words, if the matrix **A** is positive definite, its determinant will be greater than zero. However, the inverse is not true. **A** can be non-positive definite even if its determinant is positive. We have to solve (26) to find the stable domain where all of the frequencies are real.

4.2. Stability analysis of a molecular chain

A molecular chain is considered here, and the Lennard–Jones 6–12 potential in (11) is employed to describe the atomistic interaction with the energy well depth of $\varepsilon = 82.5$ aJ. Linearized stability analysis, i.e. (25), yields that the stability is governed by

$$\omega^2 - \frac{\overline{C}\kappa^2}{\rho_0} = 0 \tag{28}$$

and

$$\overline{C} = l_0\left(\varphi''(l) + \frac{\kappa_B T}{2}\frac{\varphi^{(4)}(l)}{\varphi''(l)} - \frac{\kappa_B T}{2}\left[\frac{\varphi'''(l)}{\varphi''(l)}\right]\right)^2 \tag{29}$$

It can be seen that the molecular chain becomes unstable only when $\overline{C} < 0$. The criterion for material stability of the molecular chain is

$$\varphi''(F) + \frac{\kappa_B T}{2}\frac{\varphi^{(4)}(F)}{\varphi''(F)} - \frac{\kappa_B T}{2}\left[\frac{\varphi'''(F)}{\varphi''(F)}\right]^2 \geqslant 0 \tag{30}$$

where the deformation gradient is $F = l/l_0$.

DOI: 10.1002/nme

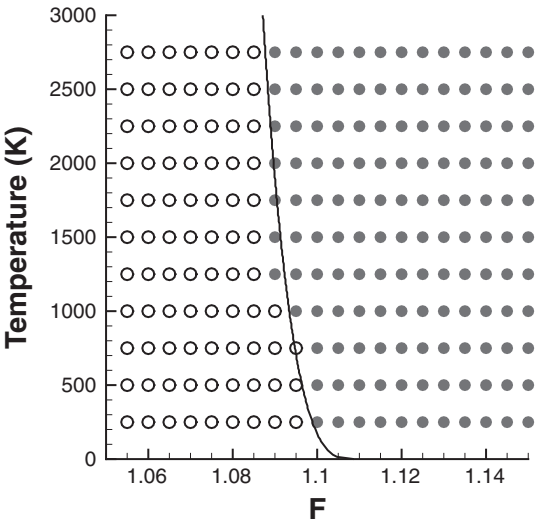

Figure 6. Stable domain of 1-D molecular chain.

Figure 6 shows the stable domain of the molecular chain based on the criterion of (30). Various deformation gradients and temperatures up to 3000 K are considered. It can be seen that the stable domain gets smaller with increasing temperature. It should be noted that the locally harmonic mode for atomic vibration might be invalid at higher temperatures that are close to the material melting temperature. In addition, molecular dynamics is conducted at selected deformation gradients and temperatures to verify the continuum material stability analysis. In the molecular dynamic model, the molecular chain contains 200 atoms. Instability occurs when the length of one bond is larger than the cutoff distance of the Lennard–Jones potential function. In other words, the molecular chain is broken. In Figure 6, solid circles represent the stable molecule chains, while the empty circles represent the unstable molecular chains. As evidenced, the molecular dynamics results support the linearized stability analysis.

4.3. Stability analysis of a two-dimensional lattice

We next consider a two-dimensional nanostructured plate with a square lattice. The Lennard–Jones potential in (11) is still used here as the potential function with the parameters of $\varepsilon = 8.25$ aJ and $l_0 = 1$ nm. Based on the TCB rule, the first tangential stiffness tensor $\overline{C}_{ijkl}$ is written as

$$\overline{C}_{ijkl} = \frac{\partial^2 w_C}{\partial F_{ij} \partial F_{kl}} + \frac{1}{V}\left(\frac{\kappa_B T}{2\overline{D}} \frac{\partial^2 \overline{D}}{\partial F_{ij} \partial F_{kl}} - \frac{\kappa_B T}{2\overline{D}^2} \frac{\partial \overline{D}}{\partial F_{ij}} \frac{\partial \overline{D}}{\partial F_{kl}} \right) \tag{31}$$

where V is the volume of the unit cell of this square lattice. The potential density, w_C, and the determinant of the dynamic matrix, $\overline{D}$, are functions of the deformation gradient, $\mathbf{F}$.

In two dimension, $n_1^0 = \cos\theta$ and $n_2^0 = \sin\theta$ and θ represents the wave front direction. For a given deformation gradient $\mathbf{F} = \begin{bmatrix} \lambda_1 & 0 \\ 0 & \lambda_2 \end{bmatrix}$ [23], if there exists ω_I such that $\mathrm{Im}(\omega_I) < 0$ for any θ,

DOI: 10.1002/nme

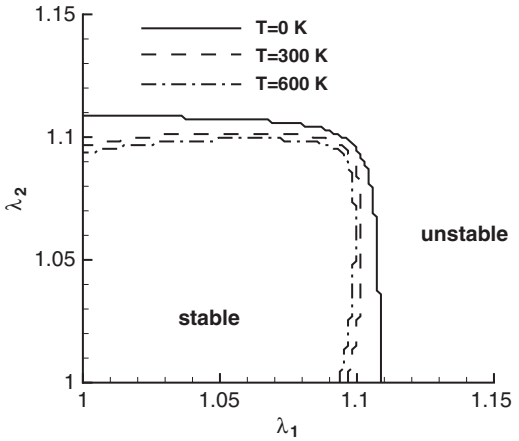

Figure 7. Stable domains at various temperatures.

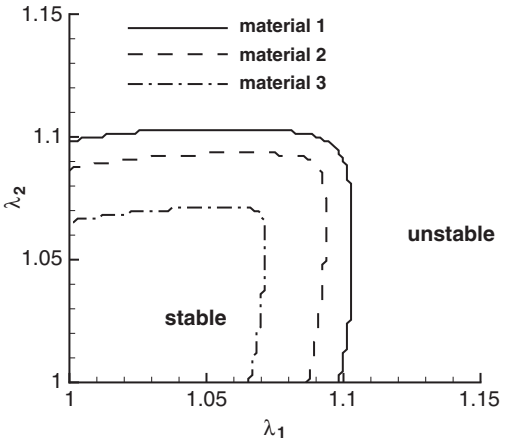

Figure 8. Stable domains of different materials at room temperature of 300 K.

the nanostructured material will be unstable. The stable domain for the material considered above is shown in Figure 7. The entire compressive domain ($0<\lambda_i \leqslant 1$) is stable. However, for sufficiently large extensional deformations, the material is unstable. It also can be seen that the stable domain is smaller at a higher temperature.

To study temperature effects on nanostructural material instability, we employ various energy well depths, ε, in the Lennard–Jones potential function (11). Three values are considered: $\varepsilon_1 = 8.25$ aJ for material 1, $\varepsilon_2 = 0.825$ aJ for material 2, and $\varepsilon_3 = 0.0825$ aJ for material 3. Obviously, material 1 is 10 times stiffer than material 2 which is 10 times stiffer than material 3. At zero temperature, those three materials have the same material stability. However, at a room temperature of 300 K, the stiffest material (material 1) has the largest stable domain, shown in Figure 8.

DOI: 10.1002/nme

5. MESHFREE PARTICLE METHODS

5.1. Meshfree particle methods

In continuum mechanics, the Galerkin weak form of the momentum conservation equation is

$$\int_{\Omega_0} \delta u_i \rho_0 \ddot{u}_i \, \mathrm{d}\Omega_0 = \int_{\Omega_0} \delta u_i \rho_0 b_i \, \mathrm{d}\Omega_0 - \int_{\Omega_0} \frac{\partial(\delta x_i)}{\partial X_j} P_{ij} \, \mathrm{d}\Omega_0 + \int_{\Gamma_0} \delta u_i \bar{t}_i \, \mathrm{d}\Gamma_0 \tag{32}$$

where ρ_0 is the initial density, $\mathbf{P}$ is the first Piola–Kirchhoff stress tensor, $\mathbf{X}$ are the material (Lagrangian) co-ordinates, $\mathbf{b}$ is the body force per unit mass, $\delta\mathbf{u}$ is the test function, $\bar{\mathbf{t}}$ is the prescribed boundary traction, and $\mathbf{u}$ is the displacement and the superposed dots denote material time derivatives. It should be noted that (32) is written under the reference configuration, Ω_0.

In meshfree particle methods, the field of displacements can be approximated as

$$\mathbf{u}^h(\mathbf{X}, t) = \sum_I w_I(\mathbf{X}) \mathbf{u}_I(t) \tag{33}$$

where $w_I(\mathbf{X})$ are called Lagrangian kernels since they are functions of the material (Lagrangian) co-ordinates. If the kernel functions are functions of the spatial (Eulerian) co-ordinates, $\mathbf{x}$, they are called Eulerian kernels. In this paper, Lagrangian kernels are applied unless otherwise noted. The Lagrangian kernel functions can be obtained from the weight function, i.e.

$$w_I(\mathbf{X}) = w(\mathbf{X} - \mathbf{X}_I) = \frac{W(\mathbf{X} - \mathbf{X}_I)}{\sum_K W(\mathbf{X} - \mathbf{X}_K)} \tag{34}$$

In our analysis, a quartic spline weight function is used:

$$W(R) = \begin{cases} 1 - 6\left(\dfrac{R}{R_0}\right)^2 + 8\left(\dfrac{R}{R_0}\right)^3 - 3\left(\dfrac{R}{R_0}\right)^4, & R \leqslant R_0 \\ 0, & R > R_0 \end{cases} \tag{35}$$

where $R = \|\mathbf{X} - \mathbf{X}_J\|$ and R_0 is the support radius of the influence domain as shown in Figure 9.

Obviously, the kernel functions reproduce the constant functions, i.e. $\sum_I w_I(\mathbf{X}) = 1$, but not the linear functions. In other words, one can find that $\sum_I w_{I,i}(\mathbf{X}) X_{Ij} \neq \delta_{ij}$. Belytschko *et al.* [18] developed a correction that enables the derivatives of the constant or linear functions to be reproduced exactly.

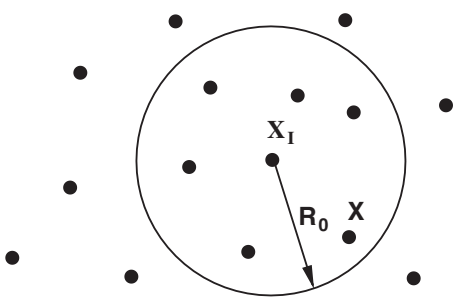

Figure 9. The domain of influence of particle $\mathbf{X}_I$.

DOI: 10.1002/nme

Substituting (33) into the weak form of (32), the following discrete equations of motion can be obtained:

$$m_I \ddot{u}_{iI} = f_{iI}^{\text{ext}} - f_{iI}^{\text{int}}, \quad m_I = \rho_0 V_I^0 \tag{36}$$

where V_I^0 is the volume associated with particle I, f_{iI}^{ext} and f_{iI}^{int} are the external and internal nodal forces, respectively, given by

$$f_{iI}^{\text{ext}} = \int_{\Omega_0} \rho_0 w_I b_i \, \mathrm{d}\Omega_0 + \int_{\Gamma_0^t} w_I \bar{t}_i \, \mathrm{d}\Gamma_0 \tag{37}$$

$$f_{iI}^{\text{int}} = \int_{\Omega_0} \frac{\partial w_I(\mathbf{X})}{\partial X_j} P_{ji} \, \mathrm{d}\Omega_0 \tag{38}$$

5.2. Numerical integration schemes

A background mesh was used in the element-free Galerkin (EFG) method [34], so that Gaussian quadrature can be used for numerical integration of (38). However, it is computationally intensive. Beissel and Belytschko [35] proposed a nodal integration scheme to reduce the computation time, where the internal forces can be calculated via

$$f_{iI}^{\text{int}} = \sum_J V_J^0 \frac{\partial w_I(\mathbf{X}_J)}{\partial X_j} P_{ji}(\mathbf{X}_J) \tag{39}$$

Another numerical integration scheme used in meshfree particle methods is the stress point integration [36]. Stress points play the same role as additional quadrature points during numerical integration. Such additional quadrature points (stress points) are also called slave points/particles, and the original particles are called master particles. The kinetic variables of stress points, such as displacements and velocities, are evaluated from the neighbouring master particles by the approximation (33).

If master particles are arranged irregularly for an object with arbitrary geometry, triangulation is usually used to construct a virtual triangular (or tetrahedral in 3-D) mesh. The stress points are then placed at the centre of triangles (or tetrahedrons). Next, the Voronoi cells are constructed for both master particles and stress points, as shown in Figure 10. The volumes of these cells are represented as $V_J^{0\text{M}}$ and $V_J^{0\text{S}}$ associated with master particles and stress points, respectively. With the stress point integration, the numerical integration for (38) can be written as:

$$\begin{aligned} f_{iI}^{\text{int}} &= \sum V_J^{0M} \frac{\partial w_I(\mathbf{X}_J^M)}{\partial X_j} P_{ji}(\mathbf{X}_J^M) \\ &\quad + \sum V_J^{0S} \frac{\partial w_I(\mathbf{X}_J^S)}{\partial X_j} P_{ji}(\mathbf{X}_J^S) \end{aligned} \tag{40}$$

5.3. Stability of meshfree particle methods

There are two sources of instability that exist in meshfree particle methods: (1) rank deficiency of the discrete equations, and (2) distortion of the material instability. The latter leads to the so-called tensile instability. Belytschko and Xiao gave a linearized stability analysis of the discrete

DOI: 10.1002/nme

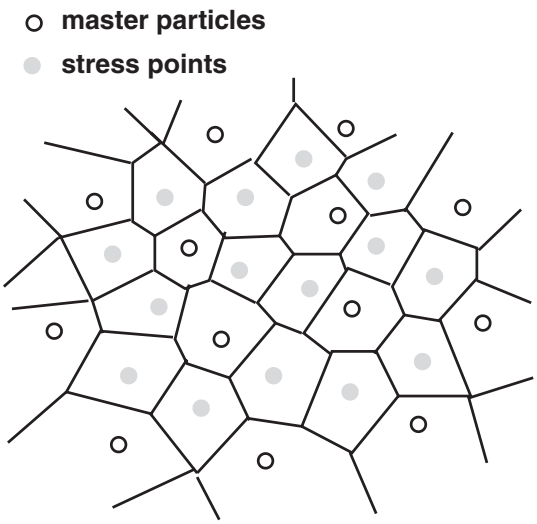

Figure 10. Voronoi cells in meshfree particle methods.

equations for the meshfree particle methods [22]; this is often called a von Neumann stability analysis.

When using the nodal integration scheme, an instability occurs in meshfree particle methods due to rank deficiency of the discretization of the divergence. This instability makes the equilibrium equations singular regardless of the value of the stress. Such instability occurs when the nodal integration scheme is employed. Stress points are inserted to eliminate this instability. However, tensile instability occurs in meshfree particle methods as long as Eulerian kernels are employed even when the stress point integration scheme is utilized. Xiao and Belytschko [23] performed material stability analysis of meshfree particle methods. They pointed out that Eulerian kernels severely distorted the material instability while Lagrangian kernels can exactly reproduce material instability. Rabczuk *et al*. [24] concluded that a meshfree particle method with Lagrangian kernels and stress point integration is a stable numerical method.

6. QUASICONTINUUM MESHFREE PARTICLE METHODS

6.1. Implementation of the TCB rule

When using meshfree particle methods for nanoscale simulation, the TCB rule results in a constitutive relationship due to molecular properties. For instance, we consider a Voronoi cell C_I associated with a particle P_I. P_I can be any master particle or stress points in the simulated domain. During the implementation of the TCB rule in meshfree particle methods, the following assumption and procedures are conducted:

- The lattice in cell C_I is assumed to be subjected to a deformation gradient as that of particle P_I. Therefore, the strain energy density at zero temperature can be calculated via a unit cell.
- All the atoms in cell C_I are assumed to have an identical harmonic vibration mode. Then, a dynamic matrix can be calculated via the unit cell for all the atoms in this cell.

DOI: 10.1002/nme

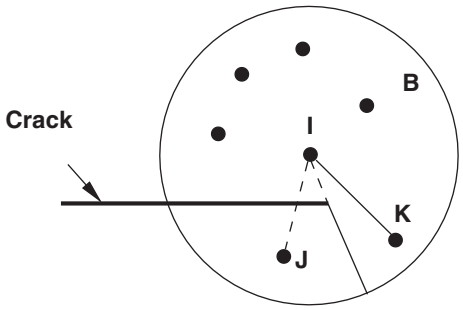

Figure 11. Visibility criterion in meshfree particle methods.

- The molecular domain in cell C_I is assumed to be at a constant temperature as that of particle P_I. The free energy density is thereafter computed via (7), and both master particles and stress points are quadrature points in meshfree particle methods.
- Once free energy density is calculated, stresses of particles can be obtained through (8) and (10). Numerical integration will be performed to compute nodal forces (37) and (38), and discrete equations (36) will be thereafter solved.

6.2. Modelling of fracture at the nanoscale

When employing FE methods in continuum models at the nanoscale, the approximated molecular lattices are always assumed to be perfect. Such hierarchical multiscale methods have difficulties in studying nanostructured material failure. Meshfree particle methods have advantages in dealing with both large deformation problems and problems with moving discontinuities such as fracture mechanics. Such advantages will benefit the developed hierarchical multiscale method in which a meshfree particle method is employed as well as the TCB rule. In this paper, we introduce a cohesive model in meshfree particle methods to model cracks at the nanoscale.

In two-dimensional problems, a crack is modelled in the meshfree particle method by defining a line segment internal to the domain as shown in Figure 11. The domains of influence for particles near the crack are truncated whenever they intersect the crack surface so that a particle on one side of the crack will not affect particles on the opposite side of the crack. This technique was called the visibility criterion by Krysl and Belytschko [37], as illustrated in Figure 11. The domain of influence can be considered as the line of sight and the crack can be considered as an opaque boundary. Whenever the line of sight meets the opaque boundary, the domain of influence is cut. In Figure 11, if we plan to search the neighbour particles for the particle I, the particle K is included but not the particle J, since the latter is not visible for the particle I due to the block of the crack. Other techniques, the diffraction method and the transparency method [38], can provide continuous and smooth approximations near non-convex boundaries. For simplification, we use the visibility criterion in this paper.

The crack propagation criterion used in our study is similar to the cohesive zone model [39]. As shown in Figure 12, two crack tips should be monitored in the cohesive zone model: one is called physical tip, which is a 'real' crack tip in physics, and the other is mathematical tip, which means it is a fictitious tip ahead of the physical one. The physical meanings of those two tips at the nanoscale are described as follows. It is known that crack propagation involves bond breakage

DOI: 10.1002/nme

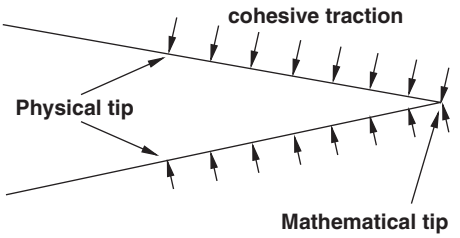

Figure 12. Cohesive zone model for crack propagation.

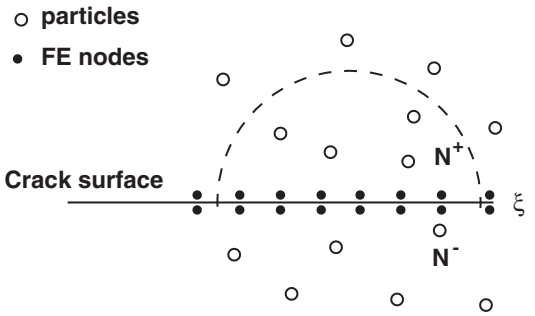

Figure 13. Projection of cohesive traction.

so that the physical tip moves to the location where bonds are broken. Such a tip can be viewed as a 'real' crack tip at the macroscale. On the other hand, the mathematical tip moves to the location where bonds become unstable. An unstable bond means that the interatomic bond force decreases while the bond length increases. Between the mathematical tip and the physical tip, there is a so-called cohesive zone, where the cohesive traction is applied on the two facets of the cohesive zone. It should be noted here that the mathematical tip is used to determine the domain of influence in meshfree particle methods via the visibility criterion. The cohesive traction, $\boldsymbol{\tau}$, are taken as external forces in meshfree particle simulation and they are derived from

$$\boldsymbol{\tau} = \frac{\partial \hat{w}_H(\boldsymbol{\Delta}, T)}{\partial \boldsymbol{\Delta}} \tag{41}$$

where $\boldsymbol{\Delta}$ is the crack opening displacement vector. $\hat{w}_H(\boldsymbol{\Delta}, T)$ is the free energy per unit length along the cohesive zone and can be calculated via the TCB rule.

In meshfree particle methods, the cohesive tractions can be projected into consistent nodal forces [39] without introducing additional degrees of freedom. In order to represent the surface geometry and calculate the cohesive traction, a parameterization must be implemented. As shown in Figure 13, we define a local co-ordinate system in the reference configuration as well as the FE points along the cohesive zone. The crack opening displacement vector $\boldsymbol{\Delta}$ may be written as

$$\boldsymbol{\Delta}(\xi) = \mathbf{u}^+(\xi) - \mathbf{u}^-(\xi) = \sum_{P \in N^+} w_p(\xi)\mathbf{u}_p - \sum_{P \in N^-} w_p(\xi)\mathbf{u}_p \tag{42}$$

where ξ are local co-ordinates; $\mathbf{u}^+$ and $\mathbf{u}^-$ are displacements of upper and lower facets of the cohesive zone, respectively; w_p is the meshfree shape function associated with particle p involved

DOI: 10.1002/nme

in the truncated neighbourhood of the FE point, $\mathbf{u}_p$ is the displacement of particle p. In a variational setting, the contribution to the virtual work from cohesive traction is

$$\delta W = \int_{\Gamma_0} \boldsymbol{\tau} \cdot \delta \boldsymbol{\Delta} \tag{43}$$

where Γ_0 is the cohesive zone in the reference configuration; and $\delta\boldsymbol{\Delta}$ is the variation in the surface opening displacement. On the other hand, in terms of the variation in the particle displacements, $\mathbf{u}_p$, the work increment due to the crack opening can be written as

$$\delta W = \sum \mathbf{f}_p \cdot \mathbf{u}_p \tag{44}$$

where $\mathbf{f}_p$ is the particle force projected from the cohesive traction $\boldsymbol{\tau}$. Therefore, the nodal force due to the cohesive traction is computed as

$$f_{pi} = \int_{\Gamma_0} \sum_j \frac{\partial \Delta_j}{\partial u_{pi}} \tau_j \, \mathrm{d}\Gamma \tag{45}$$

where

$$\frac{\partial \Delta}{\partial u_{pi}} = \begin{cases} w_p \delta_{ij} & \text{for} \quad p \in N^+ \\ -w_p \delta_{ij} & \quad\quad\; p \in N^- \end{cases} \tag{46}$$

7. EXAMPLES

7.1. Bending of a nanobeam

We first consider the bending of a nano cantilever beam containing the triangular lattice to demonstrate nanoscale simulation using the meshfree particle method. The length of the nanobeam is $L = 270\,\mathrm{nm}$ and its height is $H = 15.6\,\mathrm{nm}$. This nanobeam contains 5140 atoms. In this example, the temperature is assumed to be zero. A quadratic potential function is used to approximate the interaction between nearest atoms and it is

$$U(l) = \tfrac{1}{2} k (l - l_0)^2 \tag{47}$$

where $k = 10\,000\,\mathrm{nN/nm}$ and $l_0 = 1\,\mathrm{nm}$.

In the meshfree particle model of this nanobeam, 250 master particles are employed. During the simulation, the prescribed displacement will be increased by $\Delta d = 3.6\,\mathrm{nm}$ per calculation step. After 50 steps, the nanobeam will be bent as the final configuration shown in Figure 14 in which the stress contours from meshfree particle method simulation are compared well with those form molecular mechanics calculation.

Figure 15 illustrates the evolution of the strain energy. Meshfree particle simulations with different numbers of master particles are conducted and compared with molecular mechanics calculations. It can be seen that when even 250 master particles are employed in the meshfree particle method, the evolution of the strain energy matches with the molecular mechanics calculation very well. If 1000 or more particles are used in the simulations, the evolution of the nanobeam' strain energy is almost identical to that from the molecular mechanics calculation.

DOI: 10.1002/nme

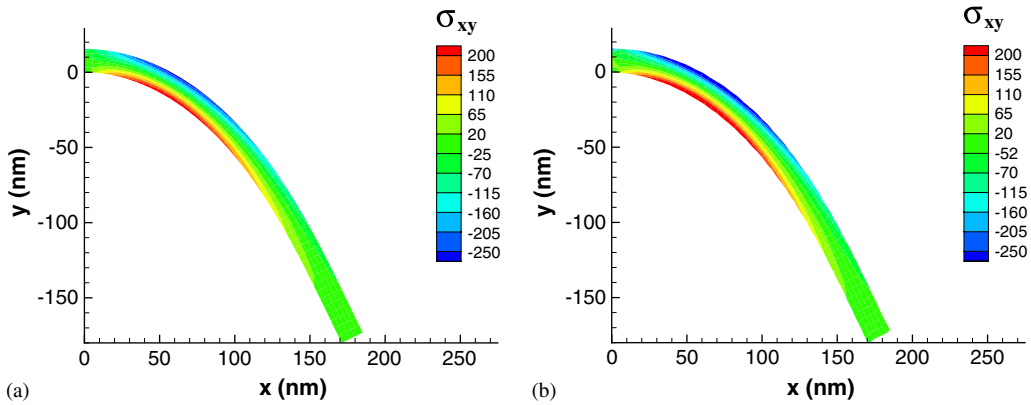

Figure 14. Deformed configurations and stress contour of the nanobeam: (a) meshfree particle method; and (b) molecular mechanics.

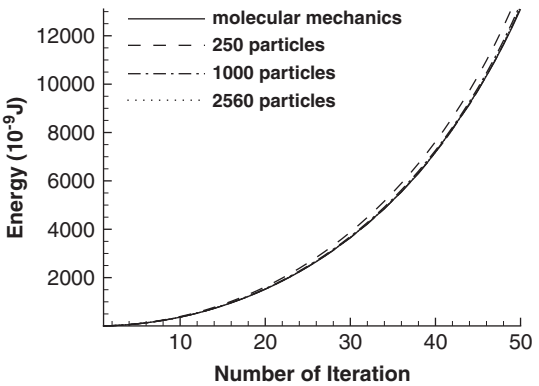

Figure 15. Comparison of evolution of the nanobeam potential.

In this example, we also study the convergence of the quasicontinuum meshfree particle method, shown in Figure 16, by using the l_2 error in displacement. The error in displacement is defined as

$$\text{Error} = \frac{\|\mathbf{u}^{\text{MM}} - \mathbf{u}^{\text{PM}}\|_2}{\|\mathbf{u}^{\text{MM}}\|_2} \tag{48}$$

where $\mathbf{u}^{\text{MM}}$ and $\mathbf{u}^{\text{PM}}$ are the atomic displacements from the molecular mechanics calculation and the meshfree particle method, respectively. Note here that one can calculate the atomic displacements from the particle displacements in the meshfree particle method based on the meshfree particle approximation. The norm is defined as follows:

$$\|u\|_2 = \left(\int_\Omega \|u\|^2\right)^{1/2} \tag{49}$$

DOI: 10.1002/nme

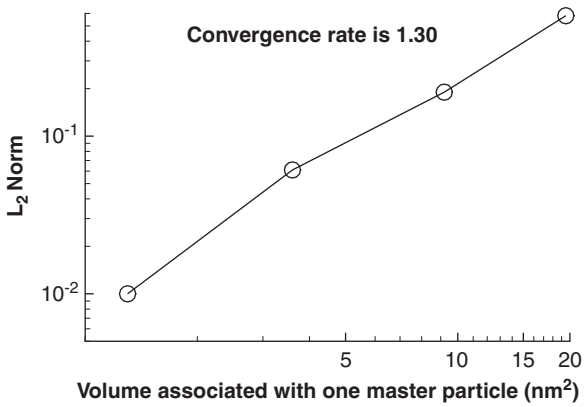

Figure 16. Convergence of the quasicontinuum meshfree particle method.

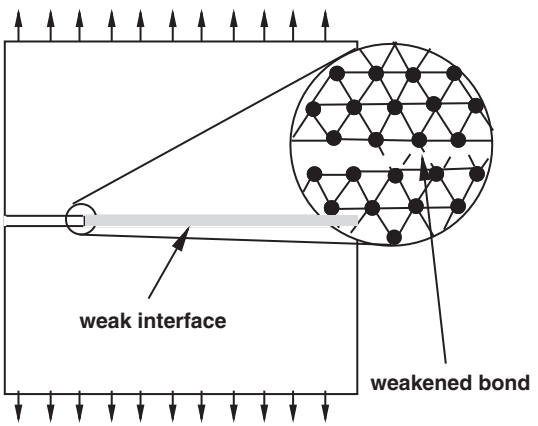

Figure 17. A nanoplate with the triangular lattice containing an initial edge crack.

7.2. Crack propagation in a nanoplate

One benefit of the quasicontinuum meshfree particle method is that it is possible to investigate the crack propagation mechanism at the nanoscale using continuum approximation. With the implementation of the TCB rule, the temperature effects can be investigated using the quasicontinuum meshfree particle method. In this example, crack propagation in a nanoplate with the triangular lattice, shown in Figure 17, is studied. We first consider the nanoplate consisting of 256 961 atoms with the following dimensions: length of 800 nm and width of 280 nm. Each atom has a mass of 1384 amu. Since the bond length is 1 nm, the density of this nano material is 2636 kg/m^3. An edge crack is initiated in the middle of the plate by taking out a number of bonds, and the initial crack length is 20 nm. For simplification, the crack is restricted to propagate along the weak interface by assuming that only weakened bonds can be broken. We employ a harmonic potential function to describe interatomic interactions between the nearest neighbouring atoms, except for weakened

DOI: 10.1002/nme

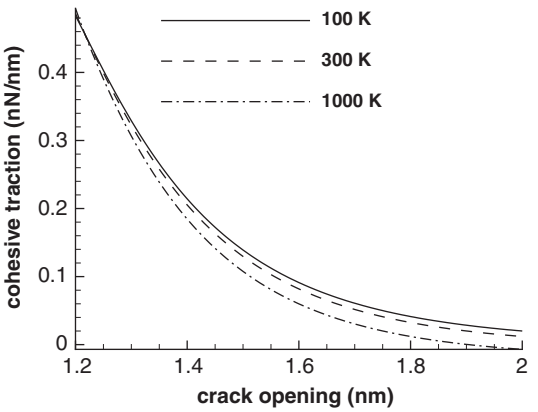

Figure 18. The relation of cohesive traction and crack opening along the weak interface.

bonds. The harmonic potential function is

$$\varphi_1(r) = \tfrac{1}{2}k(r - r_0)^2 \tag{50}$$

where the length of the undeformed bond is $r_0 = 1.0\,\text{nm}$, and the spring constant is $k = 15.6\,\text{nN/nm}$. A Lennard–Jones potential with a cutoff distance of 2.0 nm, as described in (11), is used for weakened bonds. It should be noted here that the tangential stiffness of the weakened bond is equal to the spring constant, k, so that the parameters of the Lennard–Jones potential are: $\varepsilon = 0.22\,\text{aJ}$.

The nanoplate is loaded in mode I via prescribed displacements with the strain rate of $1 \times 10^{-8}\,\text{fs}^{-1}$. We first conduct molecular dynamics simulations, the results of which will used to verify the quasicontinuum meshfree particle method. Three various temperatures—100, 300, and 1000 K—are considered. It should be noted that such a molecular structure was utilized by Buehler *et al*. [40] to demonstrate supersonic crack speed at the nanoscale. Th difference is that we employ the Berendsen thermostat [30] to maintain a constant temperature all over the plate during the molecular dynamics simulations, so, we do not observe the same phenomenon as in [40].

In the quasicontinuum meshfree particle model, there are 13 600 particles. In this example, the nodal integration scheme is used so that particles are quadrature points. Based on the assumption of the TCB rule, the free energy per length along the cohesive zone is

$$F_H = \varphi(l) + \kappa_B T \ln\left(\frac{\hbar\sqrt{\varphi''(l)}}{\kappa_B T}\right) \tag{51}$$

The cohesive traction, $\boldsymbol{\tau}$, is calculated as

$$\tau = \varphi'(l) + \frac{\kappa_B T}{2}\frac{\varphi'''(l)}{\varphi''(l)} \tag{52}$$

Figure 18 shows the relation of the cohesive traction and the crack opening along the weak interface. We can see that the traction-opening slope gets lower, i.e. the crack can propagate easier, at a higher temperature. On the other hand, the triangular lattice with the harmonic bonded potential function exhibits a special characteristic in which the Young's modulus is higher at a higher

DOI: 10.1002/nme

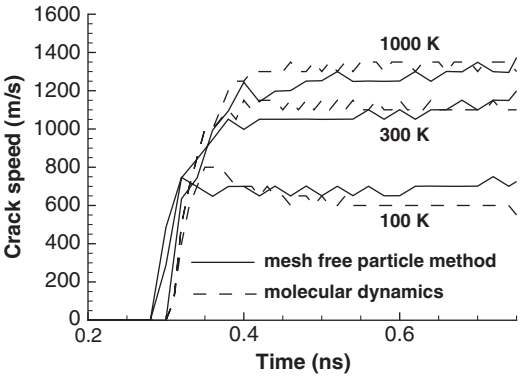

Figure 19. Comparison of crack propagation speed at different temperatures.

temperature. The moduli are 20, 25, and 36 GPa at temperatures of 100, 300, and 1000 K, respectively. The similar Young's moduli are obtained when performing molecular dynamics simulations at those three temperatures. Consequently, the Rayleigh speed is higher at a higher temperature. The crack speeds are expected to be larger at higher temperatures, as illustrated in Figure 19.

Figure 19 shows that cracks start to propagate around 0.3 ns and crack speeds become constants within 0.1 ns. The terminal constant crack speeds are 600, 1100, and 1350 m/s at 100, 300, and 1000 K, respectively. All the calculated crack speeds are lower than the Rayleigh wave speeds. Figure 19 also shows that the same phenomenon can be observed when performing molecular dynamics simulations.

Although a globally constant temperature was assumed in the above simulations, the continuum approximations with the TCB rule can deal with the object in a temperature field. Since it is assumed that atoms have the same harmonic vibration mode locally in the TCB rule, the free energy can be evaluated at the discretized particles with a locally constant temperature in the continuum approximations. Here, we investigate crack propagation in a large nanoplate with a length of 1600 nm and a width of 280 nm. The nanoplate is subject to a linear temperature field from 100 to 1000 K along its longitudinal direction. Consequently, the crack will propagate from a low temperature region to a high temperature region, and the crack speed will be linearly increased, as illustrated in Figure 20.

7.3. Nanoindentation

Nanoindentation is similar to conventional hardness testing performed on the nanoscale. The force required to press a diamond indenter into a material is measured as a function of indentation depth. Force–depth curves obtained during indenting indicate material properties, such as elastic modulus and hardness. In this example, a nanoscale indenter with the radius of 100 nm is pressed into a crystalline with the simple cubic lattice. Lennard–Jones potential, as described in (11) with $l_0 = 1$ nm and $\varepsilon = 8.25$ aJ, is employed for describing interaction between nearest atoms in the lattice. The mass of each atom is 60 amu. The crystalline has the dimensions of 500 nm $\times$ 500 nm $\times$ 250 nm and contains 65 millions atoms. Therefore, the simulation of nanoindentation is especially appealing for nanoscale continuum approximation since the experimental systems remain larger than the biggest model that can be handled by molecular dynamics. Within the quasicontinuum meshfree

DOI: 10.1002/nme

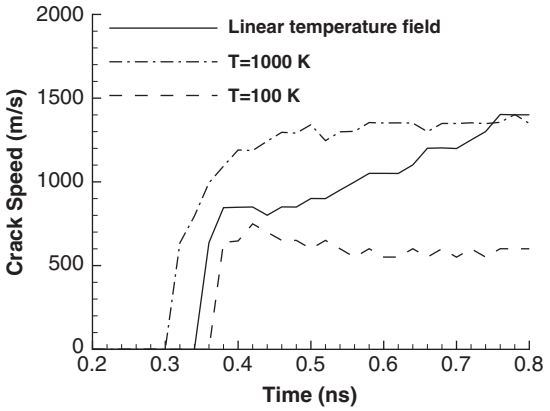

Figure 20. Crack propagation speed in linear temperature field.

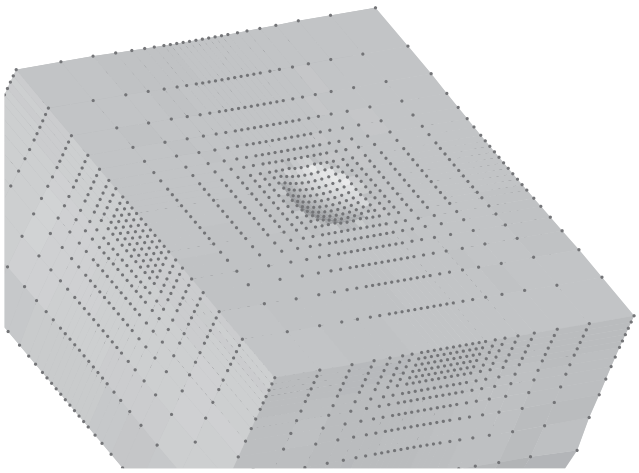

Figure 21. Simulation of nanoindentation using the quasicontinuum meshfree particle method.

particle model, 8125 particles are used to simulate this nanoindentation problem. The indenter is assumed to be rigid in this example and the deformed configuration of the nanoscale crystalline material is shown in Figure 21.

Figure 22 illustrates the force–depth relations at various temperatures. It can be seen that higher temperature results in lower force loaded on the indenter to reach the same depth. Here we assume that no dislocation occurs so that there are no kinks appearing on the force–depth curves as demonstrated in molecular or multiscale simulations [41].

In addition, we investigate the temperature effects on the force loaded on indenters for different materials. We choose different energy well depths, ε, in the Lennard–Jones potential function (11) so that the corresponding material stiffnesses are different. To reach the depth of 1 nm, the force applied on the indenter decreases when temperature increases. Figure 23 shows that the change of

DOI: 10.1002/nme

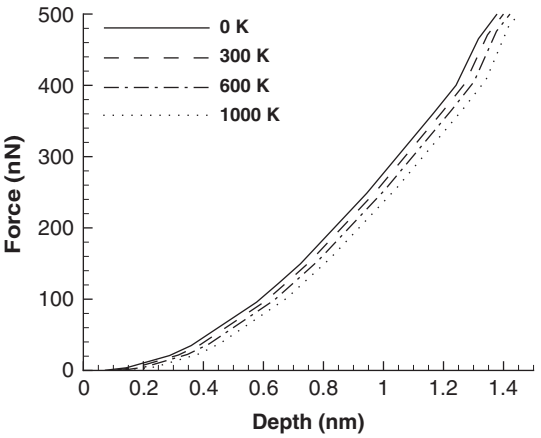

Figure 22. Force–depth relations at various temperatures.

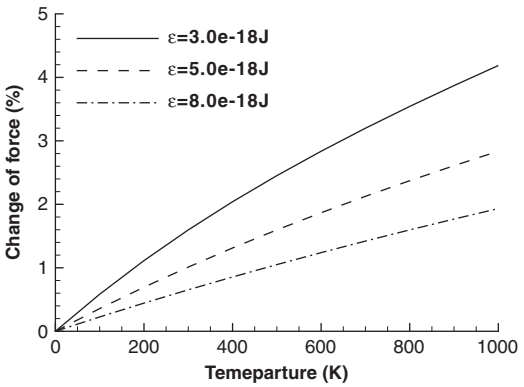

Figure 23. Comparison of temperature effects on the force loaded on indenters for different materials when the depth is 1 nm.

force is larger if the material stiffness is smaller. We conclude that temperature effects are more significant on hardness of material with smaller stiffness.

8. CONCLUSIONS

It has been known that temperature has significant effects on material behaviours at the nanoscale. Although multiscale methods can overcome the limitations of length/time scale associated with molecular dynamics, they have difficulty investigating temperature-dependent physical phenomena since most homogenization techniques have an assumption of zero temperature. The TCB rule developed in this paper can solve the above issue. The TCB rule assumes that atoms have locally harmonic motion and considers the free energy in which temperature effects are included.

DOI: 10.1002/nme

Therefore, the continuum-level stresses calculated from the free energy density instead of the strain energy density are temperature dependent. Stress analyses of several crystalline solids verified the TCB rule by comparing continuum-level Cauchy stresses with atomic-level Cauchy stresses from molecular dynamics simulation. We also found that material stability of nanostructured materials is temperature dependent. Stiffer materials can sustain larger deformation than softer materials at the same temperature. In addition, we implemented the TCB rule into meshfree particle methods, and the results from quasicontinuum meshfree particle simulations compared well with those from molecular simulations. Furthermore, the crack propagation at the nanoscale can be simulated using quasicontinuum meshfree particle methods with a cohesive crack model. It should be noted that most examples studied in this paper contained fictitious molecular structures, such as the triangular lattice or the simple cubic lattice. Those lattices were chosen mainly for verification of the proposed homogenization technique and application of the developed quasicontinuum meshfree particle method. Obviously, the framework described in this paper can be easily extended to study practical problems of nanostructured materials, which is the direction of our future research.

ACKNOWLEDGEMENTS

The author gratefully acknowledges the startup fund support from the College of Engineering and the Center for Computer-Aided Design at the University of Iowa.

REFERENCES

1. Tadmor EB, Ortiz M, Phillips R. Quasicontinuum analysis of defects in solids. *Philosophical Magazine A* 1996; **73**:1529–1563.
2. Tadmor EB, Phillips R, Ortiz M. Hierarchical modelling in the mechanics of materials. *International Journal of Solids and Structures* 2000; **37**:379–389.
3. Abraham F, Broughton J, Bernstein N, Kaxiras E. Spanning the continuum to quantum length scales in a dynamic simulation of brittle fracture. *Europhysics Letters* 1998; **44**:783–787.
4. Xiao SP, Belytschko T. A bridging domain method for coupling continua with molecular dynamics. *Computer Methods in Applied Mechanics and Engineering* 2004; **193**:1645–1669.
5. Park HS, Karpov EG, Liu WK, Klein PA. The bridging scale for two-dimensional atomistic/continuum coupling. *Philosophical Magazine* 2005; **85**(1):79–113.
6. Milstein F. In *Mechanics of Solids*, Hopkins HG, Sewell MJ (eds). Pergamon Press: Oxford, 1982.
7. Ericksen J. The Cauchy and Born hypotheses for crystals. In *Phase Transformations and Material Instabilities in Solids*, Gurtin ME (ed.). Academic Press: New York, 1984; 61–77.
8. Xiao SP, Hou WY. Fracture of vacancy-defected carbon nanotubes and their embedded nanocomposites. *Physical Review B* 2006; **73**:115406.
9. Xiao SP, Andersen DR, Han R, Hou WY. Studies of carbon nanotube-based oscillators using molecular dynamics. *Journal of Computational and Theoretical Nanoscience* 2006; **3**:142–147.
10. Najafabadi R, Srolovitz DJ. Order–disorder transitions at and segregation to (0 0 1) NI-PT surfaces. *Surface Science* 1993; **286**:104–107.
11. Garbulsky GD, Ceder G. Effect of lattice vibrations on the ordering tendencies in substitutional binary alloys. *Physical Review B* 1994; **49**:6327.
12. Shenoy V, Shenoy V, Phillips R. Finite temperature quasicontinuum methods. *Materials Research Society Symposium Proceeding* 1999; **538**:465–471.
13. Dupuy LM, Tadmor EB, Miller EM, Phillips R. Finite-temperature quasicontinuum: molecular dynamics without all the atoms. *Physical Review Letters* 2005; **95**:060202.
14. Diestler DJ. Coarse-grained descriptions of multiple scale processes in solid systems. *Physical Review B* 2002; **66**:184104.
15. Diestler DJ, Wu ZB, Zeng XC. An extension of the quasicontinuum treatment of multiscale solid systems to nonzero temperature. *Journal of Chemical Physics* 2004; **121**(19):9279–9282.

DOI: 10.1002/nme

16. Belytschko T, Liu WK, Moran B. *Nonlinear Finite Elements for Continua and Structures*. Wiley: New York, 2001.
17. Belytschko T, Krongauz Y, Organ D, Fleming M, Krysl P. Meshless methods: an overview and recent developments. *Computer Methods in Applied Mechanics and Engineering* 1996; **139**:3–47.
18. Belytschko T, Krongauz Y, Dolbow J, Gerlach C. On the completeness of meshfree particle methods. *International Journal for Numerical Methods in Engineering* 1998; **43**(5):785–793.
19. Chen JS, Roque C, Pan CH. Analysis of metal forming process based on meshless method. *Journal of Materials Processing Technology* 1998; **80**(1):642–646.
20. Krysl P, Belytschko T. The element free Galerkin method for dynamic propagation of arbitrary 3-D cracks. *International Journal for Numerical methods in Engineering* 1999; **44**(6):767–800.
21. Kim NH, Choi KK, Botkin ME. Numerical method for shape optimization using meshfree method. *Structural and Multidisciplinary Optimization* 2003; **24**(6):418–429.
22. Belytschko T, Xiao SP. Stability analysis of particle methods with corrected derivatives. *Computers and Mathematics with Applications* 2002; **43**(3–5):329–350.
23. Xiao SP, Belytschko T. Material stability analysis of particle methods. *Advances in Computational Mathematics* 2005; **23**:171–190.
24. Rabczuk T, Belytschko T, Xiao SP. Stable particle methods based on Lagrangian kernels. *Computer Methods in Applied Mechanics and Engineering* 2004; **193**:1035–1063.
25. Arroyo M, Belytschko T. An atomistic-based finite deformation membrane for single layer crystalline films. *Journal of Mechanics and Physics in Solids* 2002; **50**:1941–1977.
26. Arroyo M, Belytschko T. Finite deformation membrane based on inter-atomic potentials for the transverse mechanics of nanotubes. *Mechanics of Materials* 2003; **35**:193–215.
27. Chandler D. *Introduction to Modern Statistical Mechanics*. Oxford University Press: Oxford, 1987.
28. LeSar R, Najafabadi R, Srolovitz DJ. Finite-temperature defect properties from free-energy minimization. *Physical Review Letters* 1989; **63**(6):624–627.
29. Rickman JM, LeSar R. Free-energy calculation in material research. *Annual Review of Materials Research* 2002; **32**:195–217.
30. Berendsen HJC, Postma JPM, Gunsteren WF, DiNola A, Haak JR. Molecular dynamics with coupling to an external bath. *Journal of Chemical Physics* 1984; **81**(8):3684–3690.
31. Zhou M. A new look at the atomic level virial stress: on continuum-molecular system equivalence. *Proceedings of the Royal Society of London*, *Series A* 2003; **459**:2347–2392.
32. Tadmor EB, Smith G, Bernstein N, Kaxiras E. Mixed finite element and atomistic formulation for complex crystals. *Physical Review B* 1999; **59**(1):235–245.
33. Belytschko T, Xiao SP, Schatz GC, Ruoff R. Atomistic simulations for nanotube fracture. *Physics Review B* 2002; **65**:235430.
34. Belytschko T, Lu YY, Gu L. Element-free Galerkin methods. *International Journal for Numerical Methods in Engineering* 1994; **37**:229–256.
35. Beissel S, Belytschko T. Nodal integration of the element-free Galerkin method. *Computer Methods in Applied Mechanics and Engineering* 1996; **139**:49–74.
36. Dyka CT, Randles PW, Ingel RP. Stress points for tension instability in SPH. *International Journal for Numerical Methods in Engineering* 1997; **40**:2325–2341.
37. Krysl P, Belytschko T. The element free Galerkin method for dynamic propagation of arbitrary 3-D cracks. *International Journal for Numerical methods in Engineering* 1999; **44**(6):767–800.
38. Organ DJ, Fleming M, Belytschko T. Continuous meshless approximations for nonconvex bodies by diffraction and transparency. *Computational Mechanics* 1996; **18**:225–235.
39. Klein PA, Foulk JW, Chen EP, Wimmer SA, Gao HJ. Physics-based modelling of brittle fracture: cohesive formulations and the application of meshfree methods. *Theoretical and Applied Fracture Mechanics* 2001; **37**:99–166.
40. Buehler MJ, Abraham FF, Gao HJ. Hyperelasticity governs dynamic fracture at a critical length scale. *Nature* 2003; **426**:141–146.
41. Smith GS, Tadmor EB, Bernstein N, Kaxiras E. Multiscale simulations of silicon nanoindentation. *Acta Materialia* 2001; **49**:4089–4101.

DOI: 10.1002/nme